Supplementary Material

Response regulator PorX coordinates oligonucleotide signalling and gene expression to control the secretion of virulence factors

Claus Schmitz[1,†], Mariusz Madej[2,†*], Zuzanna Nowakowska[2], Anna Cuppari[1], Anna Jacula[2], Miroslaw Ksiazek[2], Katarzyna Mikruta[2], Jerzy Wisniewski[3], Natalia Pudelko-Malik[3], Anshu Saran[4], Natalie Zeytuni[4], Piotr Mlynarz[3], Richard J. Lamont[5], Isabel Usón[1,6], Virginijus Siksnys[7], Jan Potempa[2,5*], Maria Solà[1,*]

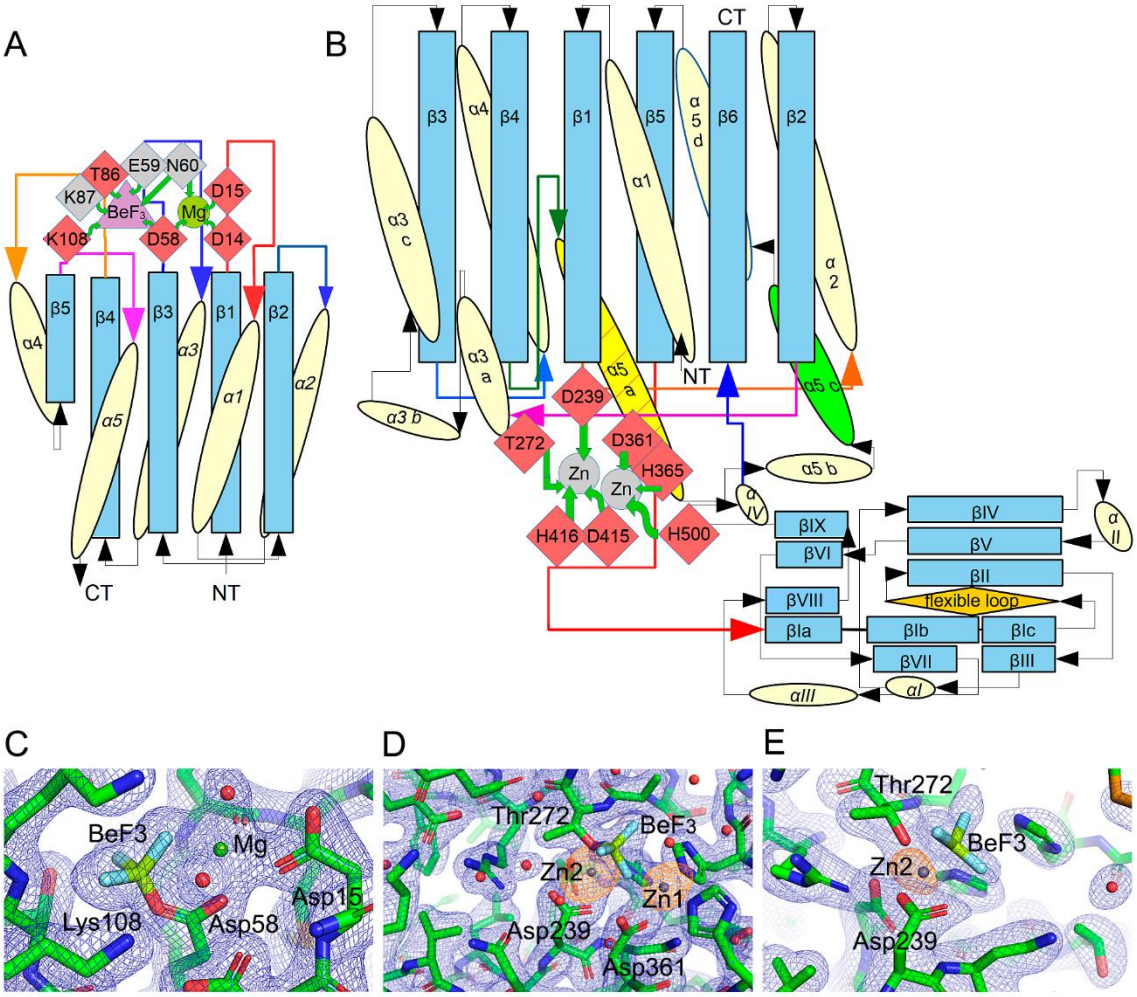

Figure S1. Topology of PorX and identification of metals at the active site. **(A)** topology of the receiver domain (RD). The β-strands of the central β-sheet are represented as blue rectangles which, in the protein sequence, alternate with α-helices, depicted as yellow ellipsoids. At the C-terminal end of the β-sheet, loops connecting β-strands and α-helices surround the active site cavity, which contains the residues that bind the activating compounds BeF_3^- and Mg^{2+}. Such contacts are formed by side-chain (red diamonds) or main-chain atoms (grey diamonds). The N-terminal and C-terminal ends are indicated (NT and CT, respectively). **(B)** topology of the PglZ domain. The α5a helix that changes conformation from an α-helix to a loop is shown in yellow with red stripes. **(C)** The active site of RD. The 2Fo-Fc electron density map is shown in blue (counter level 1.0σ map). The anomalous map collected at the Zn absorption edge, which yielded a high peak at the PglZ domain active site (see **D** and **E**), does not show any significant peak at the RD (the same occurred with Mn, data not shown). **(D)** The active site of the PglZ domain in the double-helix conformation (HH). The 2Fo-Fc electron density map is shown in blue (counter level 3). The Zn anomalous map (in orange) shows clear peaks around the positions corresponding to the two Zn ions Zn1 and Zn2 (peak height approx. 13σ for Zn1 and 40σ for Zn2). **(E)** As in (D), the electron density (2σ) and anomalous maps at the active site of the subunit with loop-helix (LH) conformation, show a single Zn ion (11σ). Representations from C to E, made with Pymol (The PyMOL Molecular Graphics System, Version 2.6.0.a.0 Open-Source, Schrödinger, LLC.), maps were previously supersampled with Coot (1).

.

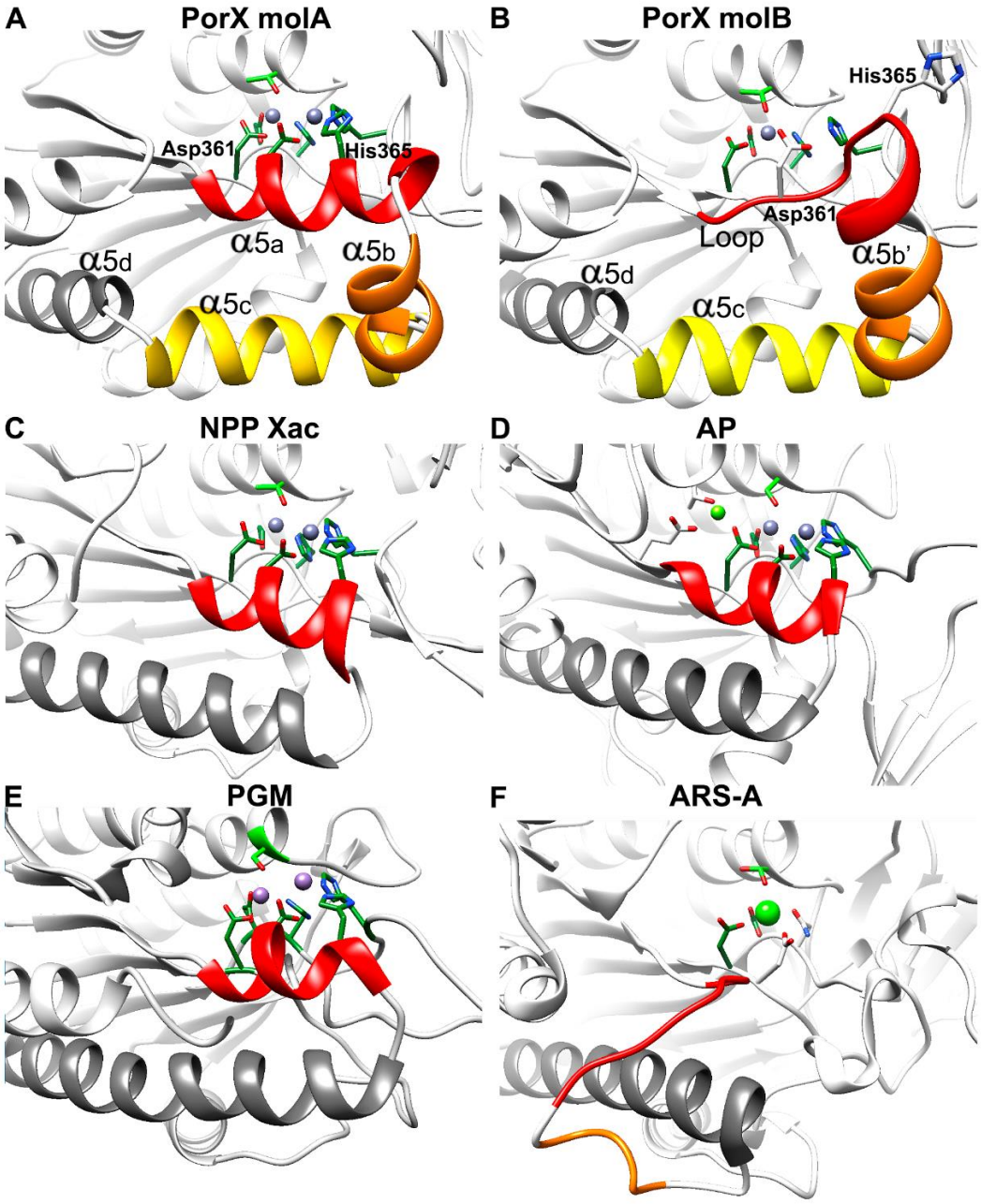

Figure S2. PorX dimer interface and the active site compared to other representative enzymes from the alkaline phosphatase superfamily (APS). **(A)** In PorX HH conformation, the two active site Zn (grey spheres) are coordinated by the APS canonical bi-metallo-core residues (in dark green sticks) which include Asp361 and His365 from PorX helix α5a (in red). **(B)** In the PorX HL conformation, helix α5 adopts a loop structure with a concomitant enlargement of downstream helix α5b', so that Asp361 and His365 (in white sticks) are relocated (see main text Fig. 3). **(C-F)** Structures of representative members of APS subclasses are shown. These enzymes do not possess helices topologically equivalent to PorX α5b (in orange) nor α5c (in yellow). Instead, they feature an elongated helix (in grey) that matches PorX α5d at the C-terminus, and do not dimerize by this surface. The representatives include (C) nucleotide pyrophosphatase/phosphodiesterase from *Xanthomonas citri* (NPP; PDB code 2GSN); (D) alkaline phosphatase from *E. coli* (AP, PDB code 1B8J) including a canonical Mg (grey sphere);

(D) phosphoglycerate mutase from yeast (PGM, PDB code 3PGM), which contains two Mn ions (violet spheres); (F) and human arylsulfatase-A (ARS-A, PDB code 1N2K) with a single catalytic Ca (green sphere) at the active site. The nucleophilic acceptor (PorX Thr272, which is not required for Zn coordination) is commonly Thr in NPPs, Ser in APs and Thr or Ser in phosphotransferases/ phosphatemutases, and formyl-Gly in arylsulfatases.

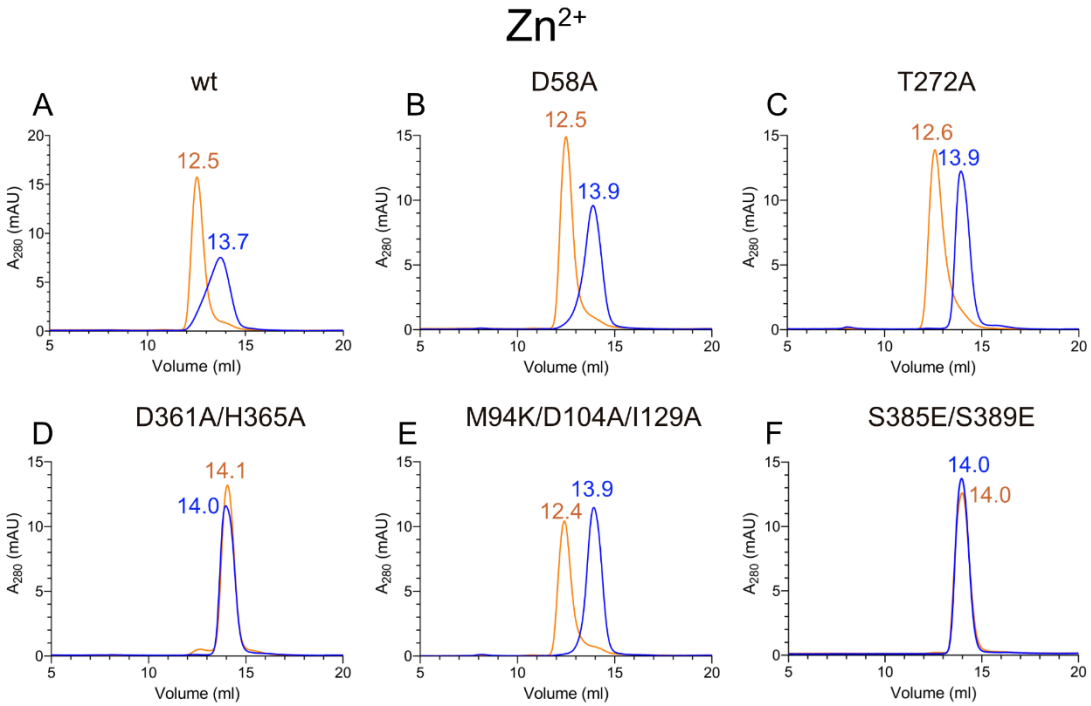

Figure S3. Analysis of PorX structure-based mutants incubated with Zn^{2+} by size-exclusion chromatography. The profiles represent PorX structure-based mutants at the RD or PglZ domain active sites or at domain interfaces following incubation with Zn^{2+} (orange curves) and corresponding non-incubated controls (blue curves). **(A)** Wild-type PorX. **(B)** D58A mutated at the RD phosphorylation site. **(C)** T272A mutated at the PglZ domain active site. **(D)** D361A/H365A with mutated Zn-coordinating amino acids at the PglZ active site. **(E)** M94K/D104A/I129A mutated at the RD dimer interface. **(F)** S385E/S389E mutated at the PglZ domain dimer interface. Elution volumes are indicated above each peak.

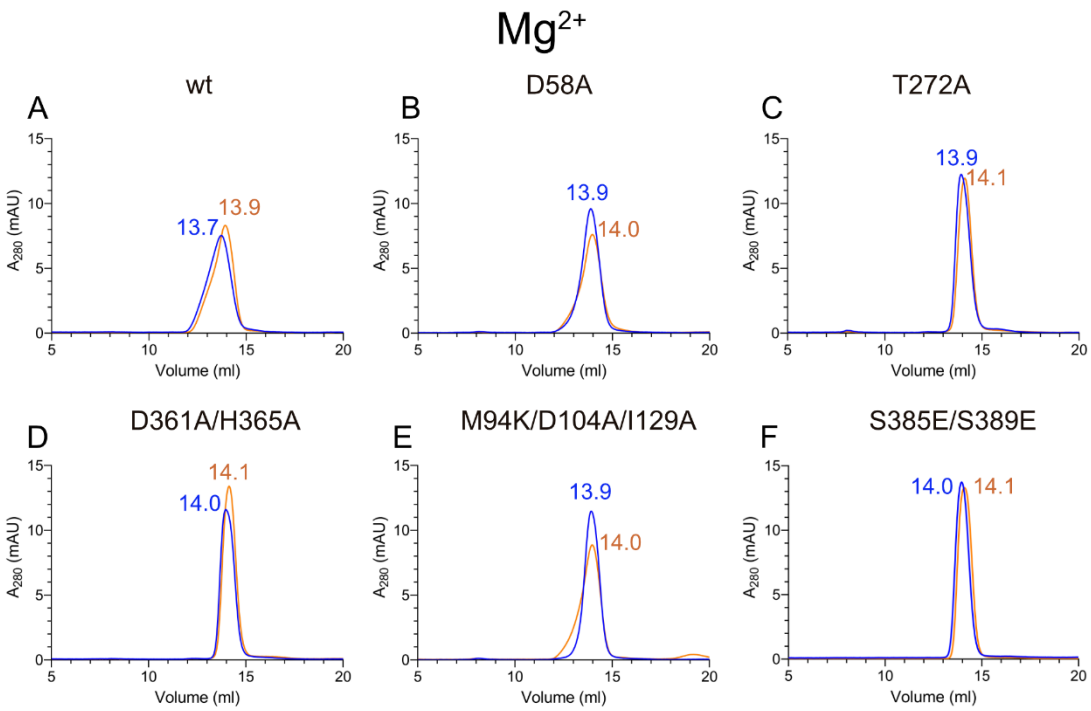

Figure S4. Analysis of PorX structure-based mutants incubated with Mg^{2+} by size-exclusion chromatography. The profiles represent PorX structure-based mutants at the RD or PglZ domain active sites or at domain interfaces following incubation with Mg^{2+} (orange curves) and corresponding non-incubated controls (blue curves). **(A)** Wild-type PorX. **(B)** D58A mutated at the RD phosphorylation site. **(C)** T272A mutated at the PglZ domain active site. **(D)** D361A/H365A with mutated Zn-coordinating amino acids at the PglZ active site. **(E)** M94K/D104A/I129A mutated at the RD dimer interface. **(F)** S385E/S389E mutated at the PglZ domain dimer interface. Elution volumes are indicated above each peak.

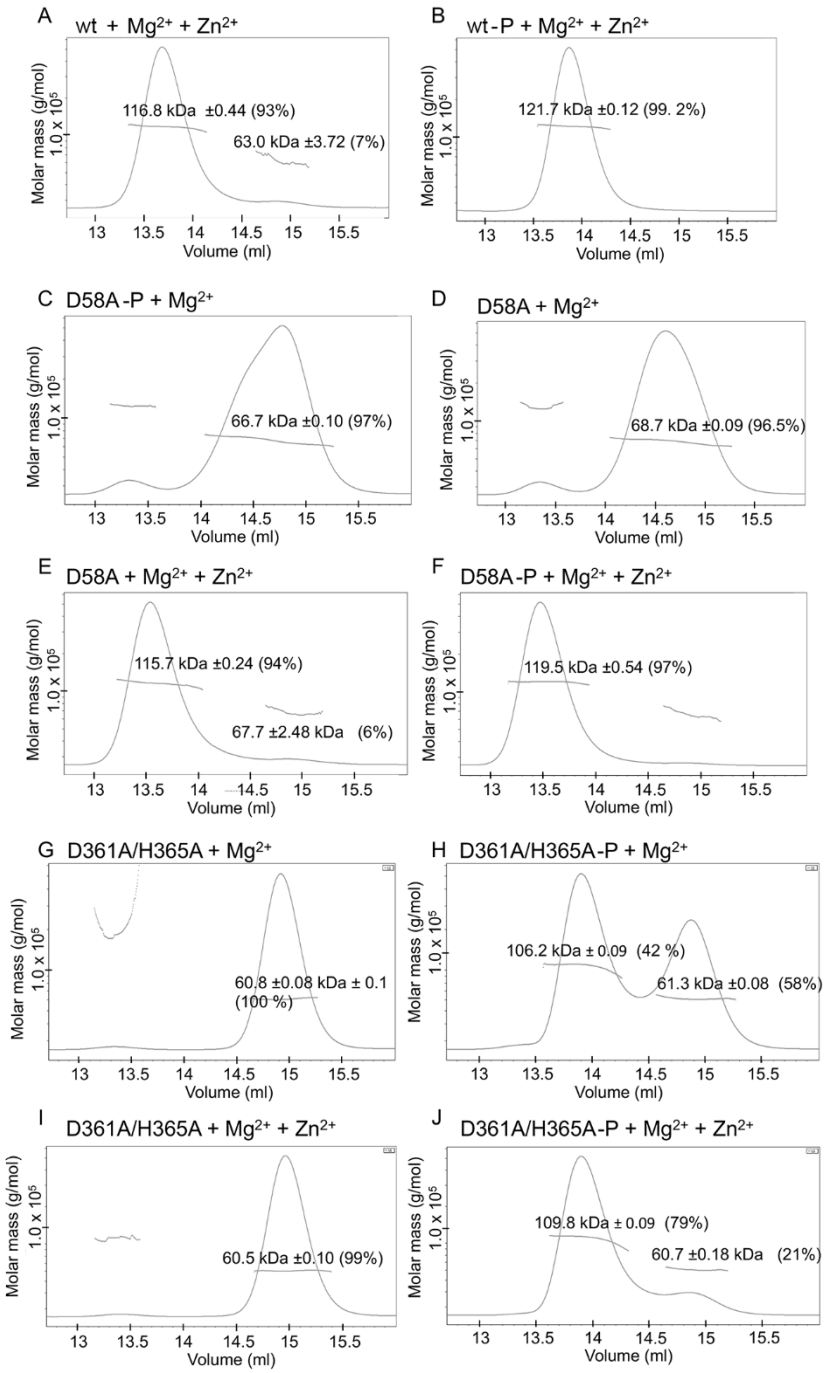

Figure S5. **SEC-MALLS analysis to determine the absolute MW of PorX dimers induced by Zn^{2+} or phosphorylation and of variants mutated at the metal binding sites.** The proportion of protein under the peak is shown as a percentage (Suppl. Table S3). All samples and buffers contained 15 µM $MgCl_2$ (+Mg^{2+}). **(A)** Wild-type PorX incubated with $ZnCl_2$. **(B)** Phosphorylated wild-type (wt-P) and $ZnCl_2$. **(C)** D58A incubated with AcP (D58A-P). **(D)** D58A. **(E)** D58A incubated with $ZnCl_2$. **(F)** D58A incubated with AcP (+AcP) and $ZnCl_2$. **(G)** D361A/H365A. **(H)** D361A/H365A incubated with AcP (D361A/H365A-P). **(I)** D361A/H365A incubated with $ZnCl_2$. **(J)** D361A/H365A incubated with AcP (D361A/H365A-P) and $ZnCl_2$.

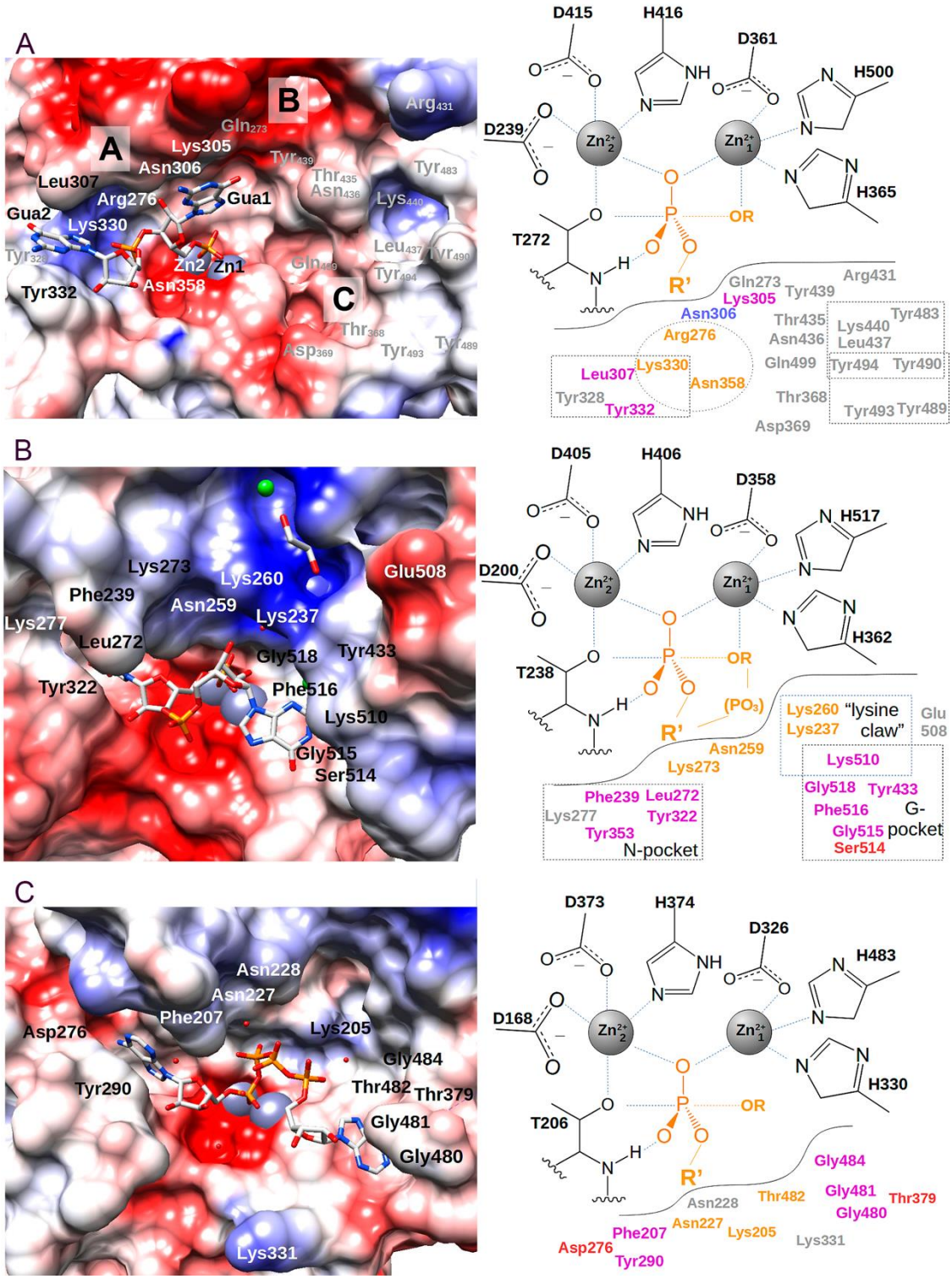

Figure S6. The ligand-bound active site of PorX and its closest structural homologs. (A) Left, Representation of the electrostatic potential (electropositive in blue, electronegative in red) on a Connolly surface of the active site of PorX T272A bound to pGpG (shown as sticks). The pGpG guanines (Gua1 and Gua2) are indicated. Labelled residues belong to the active site or are in close proximity. A, B and C labels indicate wide active site sub-pockets. The ionic radius of Zn^{2+} atoms was set to 1.9 Å. **Right**, Coordination of Zn^{2+} ions and phosphate binding at the PorX active site follow the canonical alkaline phosphatase transition-state intermediate. Amino acids coordinating the activated phosphate are labelled in orange, and hydrophobic or electro-negative/positive contacts to nucleotides are labelled in magenta or red/blue, respectively.

Labels in grey correspond to residues in close proximity. Hydrophobic sub-pockets are indicated as doted rectangles, and the α-phosphate binding site of pGpG is encircled. Residues Thr435 and Asn346 separate the B and C sub-pockets and are part of the highly flexible loop Gly429–Arg438 of the CAP domain. **(B) Left,** Electrostatic potential represented on a Connolly surface of ENPP1 bound to pApG (represented as sticks) (2). Interacting residues are represented as in panel (A). **Right**, As in panel (A) but for ENPP1-pApG. **(C) Left and right panels**, Same as in (B), here for ENPP3 bound to Ap4A (3).

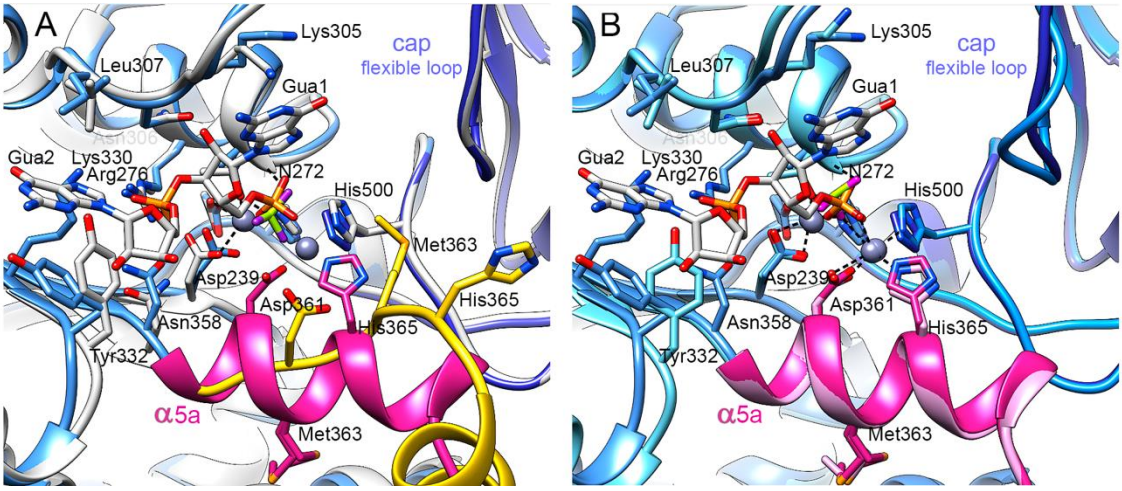

Figure S7. Binding of pGpG does not induce major structural changes. (A) Comparison between the active sites of PorX bound to pGpG (in dark blue ribbons) with the active site of the unbound protein in conformation LH (white ribbons). Helix α5 is indicated and shown in magenta. The loop from the L conformation is shown in yellow. The flexible loop at the cap domain is indicated. **(B)** Comparison between the active sites of PorX/pGpG complex with free PorX in HH conformation (light blue ribbons**)**. Helix α5a is indicated and shown in magenta (PorX/pGpG complex) or pink (free PorX). The flexible loop at the cap domain is indicated. Note the rotation of Tyr332 to perform a stacking interaction with the second guanine of pGpG (Gua2).

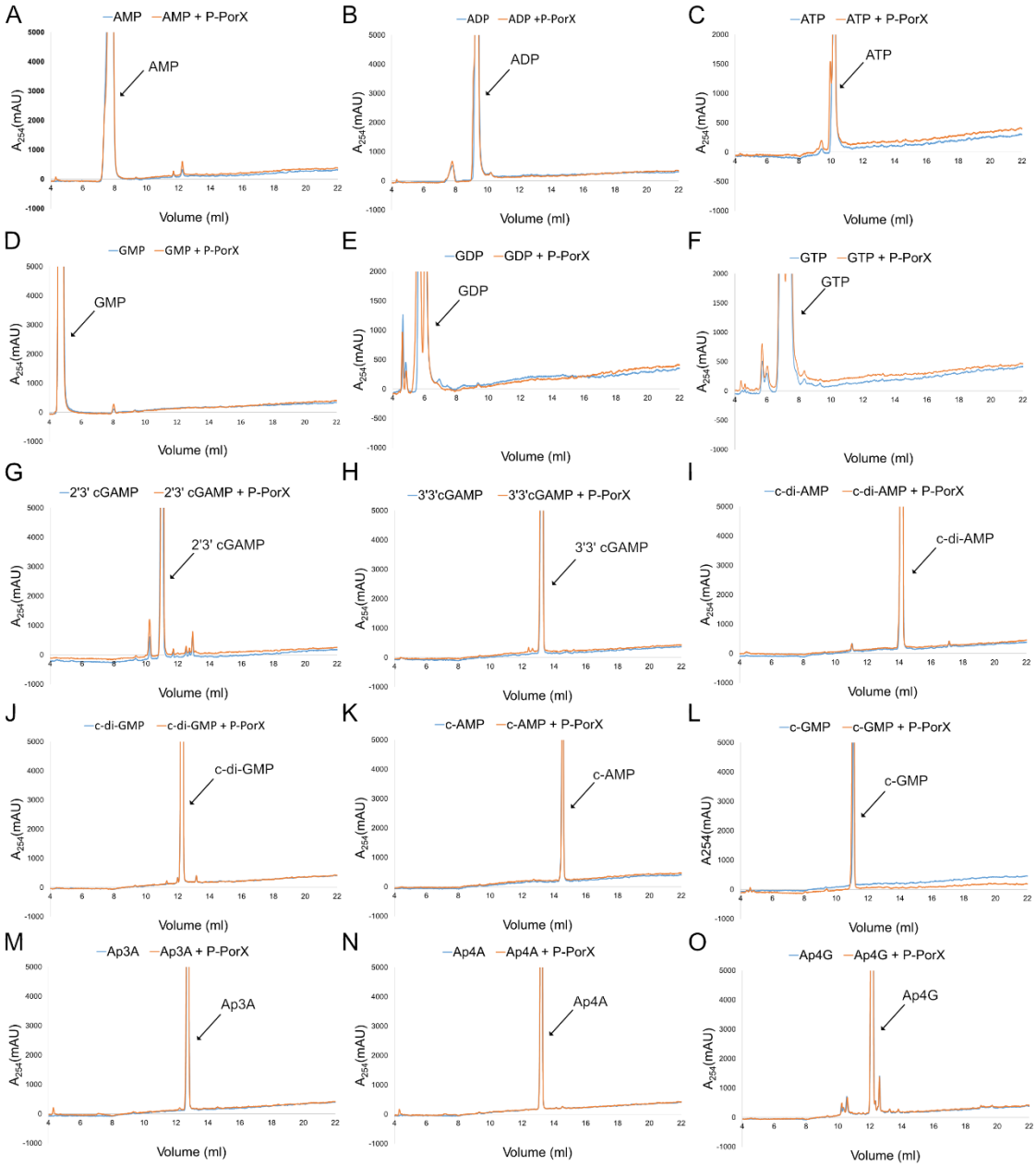

Figure S8. HPLC analysis of nucleotide cleavage by PorX. The cleavage of the nucleotide indicated in each panel (A to O) is shown following the incubation of nucleotides with phosphorylated P-PorX (orange curves) or in reaction buffer without PorX (blue curves). The orange and blue curves overlap due to the lack of cleavage.

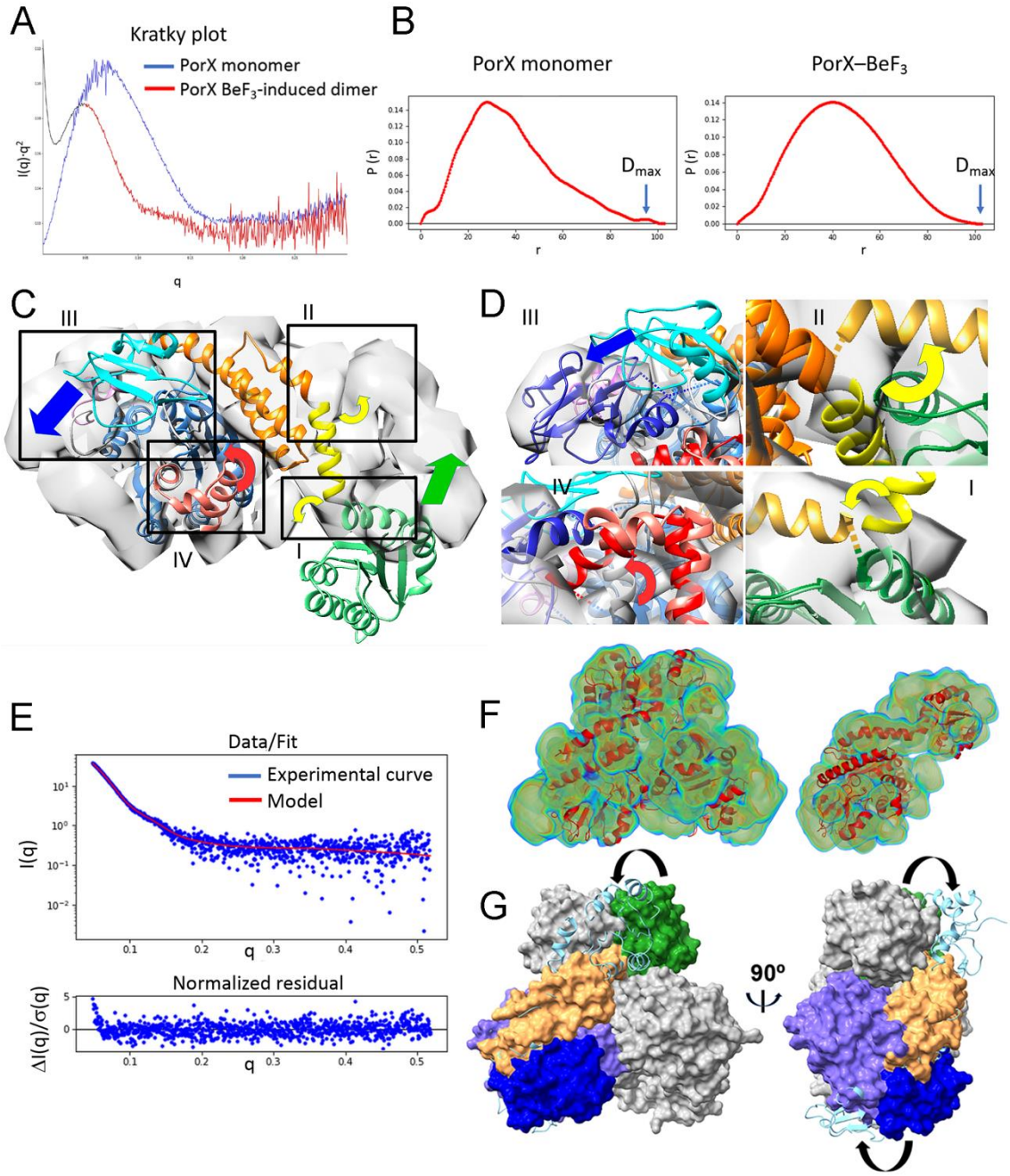

Figure S9. Analysis of PorX monomers and PorX-BeF_3 dimers in solution by small-angle X-ray scattering (SAXS). **(A)** The Kratky plots of the monomer (blue curve) and BeF_3-induced dimer (red curve) show a bell shape indicating a compacted structure. Note that data at low q from the dimeric dataset, shown in black, indicate intramolecular interactions for the dimer and were discarded. **(B)** Pairwise distance distribution calculated from the experimental SAXS curve of the monomer (left panel) and BeF_3-induced dimer. In both cases the P(r) displays a smooth decrease towards a D_{max} value of approximately 100 Å. **(C)** Superposition of the crystallographic PorX monomer onto the SAXS electron density and remodelling. While the PglZ catalytic subdomain (in deep blue) and helices 2 and 3 of the helical bundle (in orange) fit the SAXS density well, the receiver domain (in green, frame I) and the first helix of the helical bundle (in yellow, II) do not. Arrows with the corresponding colours show the displacements. Further, the PglZ cap subdomain needed to be largely displaced to fit the density (in cyan, III), as also required by the

dimerization interface region (in red, IV). **(D)** Reorientation of domains of PorX dimer subunit LH to fit the SAXS volume, superposed onto the final model. Same colours as in (C). Arrows in the same colour as the domains indicate the repositioning of the RD (I) by two consecutive remarkable bends of helical bundle helix 1 (II), the cap subdomain (III), and the interface region that shows very weak electron density, which indicates high flexibility (IV). **(E)** The crystallographic dimer fitted the experimental PorX-BeF_3 SAXS curve with a χ^2 of 1.8. **(F)** The low-resolution data were discarded for PorX-BeF_3, but a good indirect Fourier transform (IFT) could be calculated generating detailed *ab initio* electron density reconstruction consistent with the crystallographic dimer structure. **(G)** Orthogonal views superposition of the SAXS monomer (sky blue ribbons) onto crystallographic monomer A (RD in green, helical bindle domain in orange, PglZ domain in violet, CAP domain in dark blue, monomer B in grey). The reorientation of the RD and CAP domain is indicated with black curved arrows.

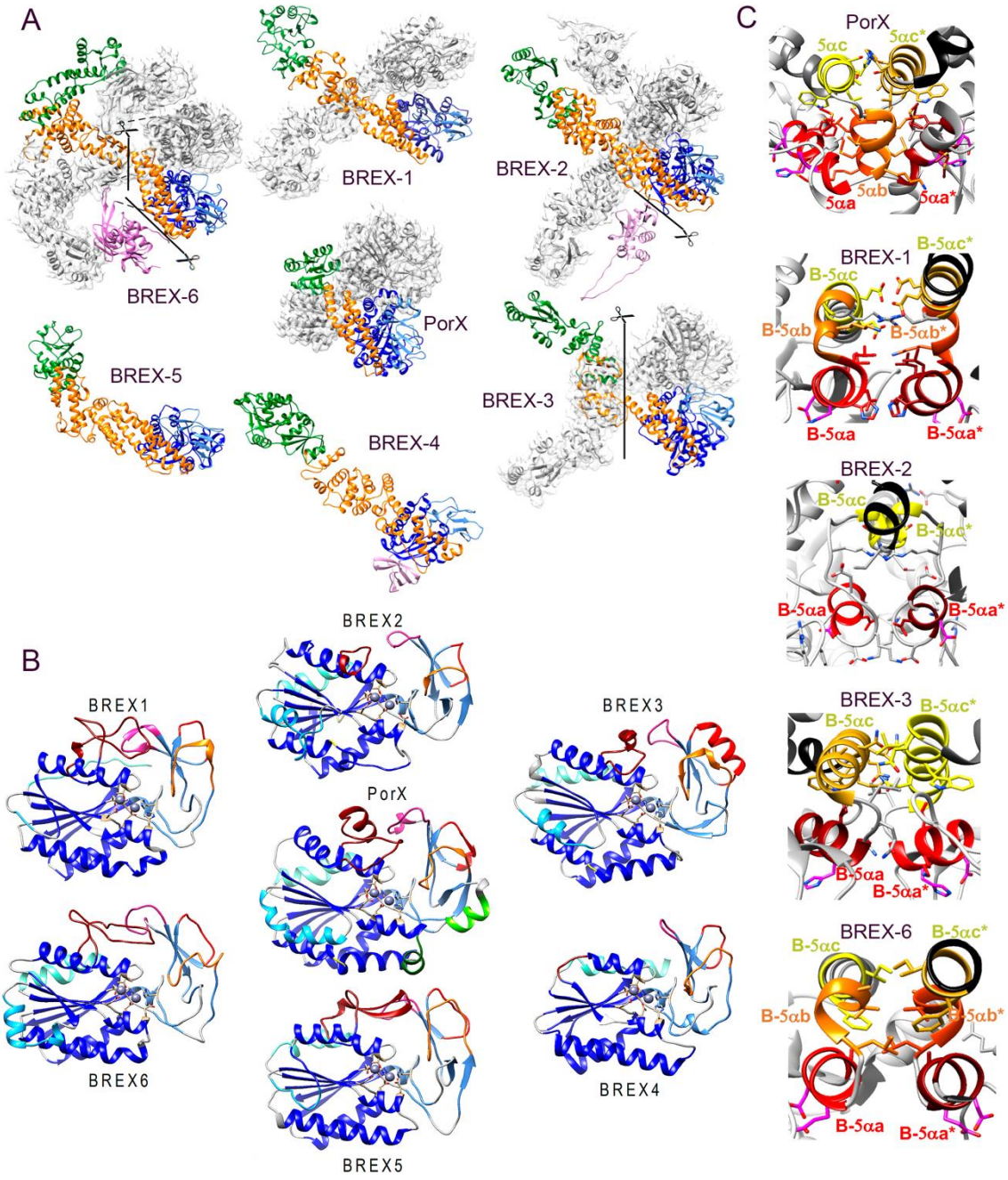

Figure S10: Comparison of the domain architectures of PorX (this work) with AlphaFold-predicted models of PglZ-containing BREX 1–6 proteins. **(A)** BREX-1 to BREX-6 (BREX_PglZ_1_B/NF033450, BREX_PglZ_2/NF033446, BREX_PglZ_3/NF033449, BREX_PglZ_4/NF033445, BREX_PglZ_5/ NF033444 and BREX_PglZ_6/NF033443) are represented around the PorX dimer (GenBank BAG33538.1) for an overall structural comparison. The PorX RD and BREX N-terminal domains are coloured green, HBDs in orange, PglZ domains in blue, and additional CT domains in violet. Dimer prediction with AlphaFold (second subunit in grey) showed an interface similar to that of PorX, except for BREX-4 and BREX-5. Scissors indicate an arbitrary connection between domains that were predicted independently due to the limited maximum number of residues (BREX-1, 3 and 6). **(B)** The AlphaFold-predicted PglZ domains from BREX-1 to BREX-6 compared with the crystallized PglZ

domain of PorX (centre). The overall fold including the central β-sheets and active site core architecture of the proteins is conserved. Minor differences are found in α1 (aquamarine) and α4 (sky blue), the last one missing in BREX-1 and BREX-4 together with α3b, 3c and β4. Further differences are found at α3b-α3c (dark red) that connects the loop that binds pGpG in PorX, as well as the interaction of this loop with the cap subdomain (CAPα2 with the following loop in magenta). CAPβ1c and the flexible loop (orange) are predicted to build an additional β-strand in the main sheet in some of the BREX models. CAPβ3 with CAPα1 (red) do not form a second sheet with CAPβ1c, but are predicted to form a loop or elongated helix in BREX-3. Two unique folds in PorX are CAPα3 (light green) and α5b (dark green). The kink between helices α5c and α5d aiding in dimerization of PorX (in yellow) is conserved in BREX-2 and BREX-3. **(C)** The dimerization interface of PorX (in HH conformation) compared to the PglZ interface of dimeric BREX AlphaFold models. Interacting helices between monomers in PorX, both in the HH conformation (see main text), and AlphaFold-predicted BREX dimers. PorX helix α5a and their equivalents in BREX proteins is coloured in red, α5b in orange, α5c in yellow, and α5d in black. The ribbons of one monomer are depicted in lighter colours than the other. Zn coordinating residues (D361 and H365 in PorX) and their equivalents in BREXs are coloured in magenta. The predicted BREX dimer interfaces involve the same area as in PorX, yet with different helical arrangements and contacts.

TABLES

Supplementary Table 1. Primers used in this study.

Name	**Sequence (5'→3')**
PorX_pGEX_BamHI_F	acgggatccatggaaaaaaacatg
PorX_pGEX_SalI_R	caggtcgacttacttgggttg
PorX_D58A_F	atcgtattcctcgccgagaacatgcccggcatcgg
PorX_D58A_R	ctcggcgaggaatacgatgtcgaagtcgttattttgcacggc
PorX_I129A_F	cagcagcacagtatcgcgagcgaaaccacgaac
PorX_I129A_R	gttcgtggtttcgctcgcgatactgtgctgctg
PorX_T272A_F	ctgccgacagcggcccaatatgcacgcaatgccatctt
PorX_T272A_R	ttgggccgctgtcggcaggatggacaggtacatatcttcttcgaa
PorX_M94K_D104A_F	aaaacacaagccatcgggggaaagatagcggcctacctcatcaaaccggtgaat
PorX_M94K_D104A_R	ggccgctatctttcccccgatggcttgtgttttgatatgctcctcttcgctttt
PorX_D361A_H365A_F	tggccatgatgtcggccgctcgtactgatagcaagatgatt
PorX_D361A_H365A_R	gcggccgacatcatggccacgaagttcaggactatcacat
PorX_S385E_S389E_F	gaactgacgaaggaatggttcaagcattcgactacctac
PorX_S385E_S389E_R	ttccttcgtcagttcgcgataggctgcttcgttg

Supplementary Table 2. Plasmids used in this study.

Plasmid	**Relevant features**	**Source**
pGEX-6P-1	*E. coli* expression vector, Ap^R, contains GST-tag for purification	Cytiva
PorX-pGEX-6P-1	master plasmid for expression and purification of full-length *porX* gene (*pg0928*) and mutagenesis studies	This study
PorX-D58A	plasmid containing substitution of DNA coding Asp for Ala in position 58 in *porX*, derivative of PorX-pGEX-6P-1	This study
PorX-T272A	plasmid containing substitution of DNA coding Thr for Ala in position 272 in *porX*, derivative of PorX-pGEX-6P-1	This study
PorX-M94K/D104A/I129A	plasmid containing substitution of DNA coding Met for Lys in position 94, Asp for Ala in position 104 and Ile for Ala in position 129 in *porX*, derivative of PorX-pGEX-6P-1	This study
PorX-D361A/H365A	plasmid containing substitution of DNA coding Asp for Ala in position 361 and His for Ala in position 365 in *porX*, derivative of PorX-pGEX-6P-1	This study
PorX-S385E/S389E	plasmid containing substitution of DNA coding Ser for Glu in positions 385 and 389 in *porX*, derivative of PorX-pGEX-6P-1	This study
PorX-S385E/S389E/D361A/H365A	plasmid containing substitution of DNA coding Ser for Glu in positions 385 and 389 in *porX*, and also substitution of DNA coding Asp for Ala in position 361 and His for Ala in position 365 in *porX*, derivative of PorX-pGEX-6P-1	This study

Supplementary Table 3. MALLS data for non-phosphorylated and phosphorylated (-P) wild-type PorX (WT) as well as the active site mutants D58A (RD) and D361A/H365A (PglZ domain), measured in the presence of $MgCl_2$, or $MgCl_2$ and $ZnCl_2$. BSA is a negative control. Mn = average number molecular weight; Mw = molecular weight determined by scattering contribution, relative to size; polydispersity is relative to heterogeneity of sizes; calculated mass = total mass of protein within each peak; mass fraction = mass of protein in a peak, relative to the total mass. Peak 1 corresponds to the highest mass fraction.

$MgCl_2$	Mn (kDa)	Mw (kDa)	Polydispersity (Mw/Mn)	Calculated mass (µg)	Mass fraction (%)
	Peak 1				
BSA	66.87 ± 0.05	66.87 ± 0.05	1.00 ± 0.00	36.45	83.11
wt	69.92 ± 0.10	70.15 ± 0.09	1.00 ± 0.00	62.23	97.55
wt-P	118.15 ± 0.17	118.21 ± 0.17	1.00 ± 0.00	48.74	80.94
D58A	68.58 ± 0.09	68.69 ± 0.09	1.00 ± 0.00	61.23	96.50
D58A-P	66.68 ± 0.10	66.88 ± 0.10	1.00 ± 0.00	61.37	96.75
D361A/H365A	60.83 ± 0.08	60.84 ± 0.08	1.00 ± 0.00	61.84	99.65
D361A/H365A-P	61.28 ± 0.08	61.29 ± 0.08	1.00 ± 0.00	32.60	57.55
	Peak 2				
BSA	133.75 ± 0.22	133.77 ± 0.22	1.00 ± 0.00	5.70	13.00
wt	114.54 ± 0.65	114.54 ± 0.65	1.00 ± 0.01	1.29	2.02
wt-P	63.44 ± 0.24	63.47 ± 0.24	1.00 ± 0.01	11.48	19.06
D58A	128.69 ± 0.73	128.89 ± 0.74	1.00 ± 0.01	1.22	1.92
D58A-P	124.18 ± 2.43	124.19 ± 2.43	1.00 ± 0.03	1.28	2.02
D361A/H365A	198.44 ± 2.72	207.20 ± 3.06	1.04 ± 0.02	0.28	0.45
D361A/H365A-P	105.88 ± 0.09	106.23 ± 0.09	1.00 ± 0.00	24.05	42.45
$MgCl_2$, $ZnCl_2$					
	Peak 1				
BSA	65.79 ± 0.09	65.79 ± 0.09	1.00 ± 0.00	36.44	82.74
wt	116.73 ± 0.45	116.79 ± 0.44	1.00 ± 0.01	15.62	92.58
wt-P	121.63 ± 0.12	121.66 ± 0.12	1.00 ± 0.00	59.42	99.21
D58A	115.59 ± 0.24	115.71 ± 0.24	1.00 ± 0.00	14.59	94.13
D58A-P	119.54 ± 0.13	119.55 ± 0.13	1.00 ± 0.00	53.97	97.16
D361A/H365A	60.49 ± 0.10	60.49 ± 0.10	1.00 ± 0.00	56.24	99.23
D361A/H365A-P	109.34 ± 0.09	109.78 ± 0.09	1.00 ± 0.00	44.41	79.37
	Peak 2				
BSA	130.38 ± 0.35	130.42 ± 0.35	1.00 ± 0.00	6.25	14.19
wt	62.57 ± 3.76	63.00 ± 3.72	1.01 ± 0.08	1.25	7.42
wt-P	210.35 ± 2.19	210.47 ± 2.19	1.00 ± 0.01	0.47	0.79
D58A	67.74 ± 2.48	67.93 ± 2.47	1.00 ± 0.05	0.91	5.87
D58A-P	65.97 ± 1.69	66.29 ± 1.66	1.00 ± 0.04	1.58	2.84
D361A/H365A	110.96 ± 4.69	111.05 ± 4.65	1.00 ± 0.06	0.44	0.77
D361A/H365A-P	60.73 ± 0.18	60.75 ± 0.18	1.00 ± 0.00	11.54	20.63

Supplementary Table 4. Data collection and refinement statistics. Statistics for the highest resolution shell are shown in parentheses.

	PorX-BeF$_3$	***PorX-HR***	***T272A-pGpG***
Wavelength [Å]	0.97893	1.28202	0.97923
Resolution range	68.4 - 2.41 (2.50 - 2.41)	68.59 - 1.91 (1.98 - 1.91)	51.9 - 2.40 (2.49 - 2.40)
Space group	P 1	P 1	P 1 21 1
Unit cell a,b,c (Å); α, β, γ (º)	61.8 77.1 138.7 82.3 81.4 76.4	61.5 77.3 138.8 82.4 81.6 76.5	94.6 103.8 132.2 90.0 98.5 90.0
Total reflections	335929 (31630)	3157066 (314354)	1419719 (139958)
Unique reflections	92407 (8754)	186912 (18467)	98575 (9713)
Multiplicity	3.6 (3.6)	16.9 (17.0)	14.4 (14.3)
Completeness (%)	97.91 (93.11)	98.30 (96.75)	99.39 (98.28)
Mean I/sigma(I)	6.45 (0.99)	12.29 (1.24)	15.93 (0.90)
Wilson B-factor	49.34	40.57	65.79
R-merge	0.1264 (0.8829)	0.1495 (2.903)	0.1222 (3.498)
R-meas	0.149 (1.039)	0.1542 (2.991)	0.1267 (3.626)
R-pim	0.07766 (0.5407)	0.03758 (0.7175)	0.03333 (0.9475)
CC1/2	0.992 (0.613)	0.998 (0.609)	0.999 (0.635)
CC*	0.998 (0.872)	1 (0.87)	1 (0.882)
Reflections used in refinement	92121 (8743)	186867 (18463)	98355 (9684)
Reflections used for R-free	971 (82)	1877 (183)	1041 (120)
R-work	0.1857 (0.3277)	0.1588 (0.2999)	0.1937 (0.3800)
R-free	0.2155 (0.3419)	0.1920 (0.3080)	0.2230 (0.4137)
CC(work)	0.963 (0.761)	0.971 (0.773)	0.966 (0.701)
CC(free)	0.955 (0.629)	0.963 (0.771)	0.954 (0.579)
Number of non-hydrogen atoms	18453	19606	17800
macromolecules	17144	17604	17188
ligands	143	171	156
solvent	1166	1831	456
Protein residues	2054	2033	2052
RMS(bonds)	0.004	0.016	0.005
RMS(angles)	1.06	1.50	0.98
Ramachandran favored (%)	96.68	97.92	96.38
Ramachandran allowed (%)	3.32	2.08	3.62
Ramachandran outliers (%)	0.00	0.00	0.00
Rotamer outliers (%)	1.52	1.02	1.17
Clashscore	4.78	7.56	2.33
Average B-factor	61.04	58.76	89.35
macromolecules	61.20	57.75	89.37
ligands	75.33	77.36	112.28
solvent	56.84	66.73	80.85

Supplementary Table 5. Closest 20 homologous structures to the PglZ domain, with a Z-score (Z) of at least 11.5, found in the Protein Data Bank (PDB) by DALI (4). The root mean square deviation (RMSD) between C^{α} atoms is indicated for a number of aligned residue pairs (LALI number). PDBs have been ordered by protein, highest Z-scores, r.m.s.d. and lali.

Nr.	Protein	Z	Rmsd	LALI	PDB	Organism	Substrates	Function	Metal
1	PhnA, Phospho-noacetate hydrolase	17.4	3.7	247	3szy, 3t01, 1ei6, 3sz, 3t00, 3t02	S. meliloti, P. fluorescens	- Phosphonoacetate(5)	Phosphono-acetate metabolism(5)	2 x Zn^{2+}
2	ENPP5, Type I phosphodi-esterase / nucleotide pyrophos-phatase	17.3	3.4	247	5vem 5veo, 5ven	H. sapiens, M. musculus	- Hydrolyzes NAD/ NAD+ - able to hydrolyze ADP-ribose (ADPR) and UDP glucose (UDPG) - no activity with nucleotide di- and triphosphates - no lysopholipase D activity(6)	Neuronal cell communication (6)	2 x Zn^{2+}
3	ENPP4, Type I phosphodi-esterase / nucleotide pyrophos phatase	17.1	3.7	248	4lqy, 4lr2	H. sapiens,	- Hydrolyzes extracellular Ap3A into AMP and ADP and Ap4A into AMP and ATP. No ATPase activity(7)	Vascular smooth muscle cell proliferation, blood coagulation.(7)	2 x Zn^{2+}
4	Xac, nucleotide pyrophos-phatase/ phosphodi-esterase, Type I phosphodi-esterase / nucleotide pyrophos-phatase	16.9	4.0	251	2gsn, 2gso, 2rh6, 2gsu	X. citri	- NPP activity - ATP hydrolysis(8)	- not classified	2 x Zn^{2+}
5	ENPP3, Type I phosphor-diesterase / nucleotide pyrophos-phatase	16.8	3.5	245	6c01, 6f2t, 6f30, 6c02, 6f33, **6f2y**,	H. sapiens, R. norvegicus	- Hydrolyzes of extracellular nucleotides ATP, GTP, UTP and CTP - Hydrolyzes Ap3A and Ap4A, UDPGlc,	- mast cell and basophil inhibition - prevents release of inflammatory cytokines	2 x Zn^{2+}

					6c02, 6c01, 6f2v,		UDPGlcNAc and NAD+ (3)	-glycosyltrans-fer regulatory activity(3)	
6	ENPP7, Type I phosphor-diesterase / nucleotide pyrophos-phatase	16.8	3.5	247	5tcd, 5udy	H. sapiens, R. norvegi-cus	alkaline sphingomyelinase (9) - extracellular sphingomyelinase - phospholipase C activity - no nucleotide pyrophosphatase activity	- gastrointestinal sphingomyelin digestion, ceramide formation, and fatty acid absorption	2 x Zn^{2+}
7	ENPP6, Type I phosphor-diesterase / nucleotide pyrophos-phatase	16.8	3.9	246	5egh, 5ege	H. sapiens, M. musculus	- choline-specific glycerophosphodi-ester-phosphodiesterase - hydrolyzes glycerophospho-choline and lysophosphatidyl-choline(10)	- lipid metabolism	2 x Zn^{2+}
8	Snake venom phosphor-diesterase	16.7	3.5	246	5gz5, 5gz4	Naja atra atra	- Hydrolyzes ADP with high activity - weak or no activity on 5'-AMP, 5'-GMP, 3'-AMP, ATP, cAMP or cGMP(11)	- platelet aggregation inhibition	2 x Zn^{2+}
9	ENPP1, Type I phospho-diesterase / nucleotide pyrophos-phatase	16.3	3.7	247	6aek, 4gtz, 4gtw, 4b56 4gtx, 4gty, 4gtz, 4gty, 4b56 6ael, 4gtw	H. sapiens, M. musculus	NTP hydrolysis to NMP and PPi, prefers ATP, hydrolyses diadenosine polyphosphates - cleaves 3',5'-cAMP to AMP - hydrolyzes 2'-3'-cGAMP to AMP and GMP, but not 3'-3'-cGAMP - hydrolyses Ap3A (7),(12) (2,13,14)	- involved in bone mineralization and calcification of soft tissue - regulation of nucleotide levels in ER and Golgi - regulation of purinergic signaling - immune suppression by inhibiting TMEM173/STIN G and type-I interferon production(7),(12),(2)	2 x Zn^{2+}
10	ENPP2, Autotaxin	16.1	3.6	244	3wav 6w35	M. musculus,	- lysophospholipase D, hydrolyzes	- chemotaxis, microtubule	2 x Zn^{2+}

					3nkr, 3nkn, 5lia, 3nko, 6leh, 3nkq, 5m0e 5dlw, 5l0b, 5dlv, 5m7m, 5ohi, 5ijq, 5olb, 3wax, 2xr9, 5hrt, 5l0k, 3way, 5m0m, 4zg7, 5kxa, 5mhp, 4zg6, 5m0d, 5l0b, 4zg6, 5ijs, 5lqq, 5l0e, 3nkp, 4zg9	R. norvegi-cus, H. sapiens	lysophospholipids to lysophosphatidic acid - hydrolyzes sphingosylphospho-rylcholine to sphingosine-1-phosphate -Ap3A hydrolysis(7) "selectivity for lipid over nucleotide substrates "(15)	formation, neurite remodelling, prolferation and survival/apoptosis - tumor formation and metastasis [protparm](15)	
11	PafA alkaline phospha-tase	14.9	3.6	237	5tj3, 5too	E. meningo-septica	- rather unspecific alkaline phosphatase - hydrolyses NTPs to NDPs, dephosphorylates phosphate monoesters except 2',3'-cyclic AMP and myo-inositol hexakisphosphate	- periplasmatic phosphatase	2 x Zn^{2+}
12	SPAP/Alka-line phospha-tase PhoK;	14.9	3.6	246	3q3q, 5xwi, 5xwk	Sphingo-monas sp.	- phosphomonoester hydrolses (16)	- secreted enzyme	2 x Zn^{2+}

	(homolog to PafA)								
13	BT_1596, Delta 4,5-hexuronate-2-O-sulfatase	12.9	3.1	184	5g2t, 5g2u	B. thetaiotaomicron	- hydrolysis of glycosaminoglycan, chondroitin sulfate, dermatan sulfate and heparan sulfate	- Exosulfatase - nutrition accisition as human gut symbiont	none
14	Inner membrane protein YejM sulfatase domain 245-586	12.2	3.3	181	5i5h	E. coli	- hydrolysis of sulfuric esters	- unknown function	none
15	2,3-bisphosphoglycerate, independent phosphoglycerate mutase gpmI	11.7	3.8	173	2ify	B. anthracis	- Isomerization of 2- and 3-phosphoglycerate	- Glucose metabolism	2 x Mn^{2+}
16	Choline sulfatase, betC	11.6	3.1	179	6g60	S. meliloti	- hydrolyses choline-sulfate into choline	- Choline metabolism	Ca^{2+}
17	Arylsulfatase A	11.5	3.3	170	1e2s	H. sapiens	- Hydrolyzes cerebroside sulfate	- Glycosphingolipid metabolism	Ca^{2+}
18	Phosphoethanolamine transferase EptC	11.5	3.4	183	4tn0	C. jejuni	Hydrolases sulfuric esters - Phosphotransferase activity	- cell-surface modification	Zn^{2+}
19	Sulfamidase	11.5	3.3	179	4mhx	H. sapiens	- N-sulphoglucosamine sulphohydrolase	- involved in heparan sulfate degradation	Ca^{2+}
20	MRC1, probable phosphatidylethanolamine transferase	11.5	3.2	182	5lrm, 6li5, 5lrn, 5grr, 6li6, 5lrn	E. coli	- Phosphoethanolamine addition to lipid A	- provides polymyxin resistance	1 or 2xZn^{2+}

Supplementary Table 6. Kinetic parameters determined for wild-type PorX and PorX variants.

PorX + Zn^{2+} bis-*p*NPP							
	wt	D58A	T272A	D361A/ H365A	M94K/ D104A/ I129A	S385E/ S389E	S385E/S389E/ D361A/H365A
k_{cat} (sec^{-1})	0.009	0.009	ND	ND	0.011	0.003	ND
K_m (mM)	2.831	3.033	ND	ND	3.968	28.60	ND
k_{cat}/K_m (M^{-1} sec^{-1})	3.172	2.920	ND	ND	2.860	0.095	ND
P-PorX + Zn^{2+} bis-*p*NPP							
	wt	D58A	T272A	D361A/ H365A	M94K/ D104A/ I129A	S385E/ S389E	S385E/S389E/ D361A/H365A
k_{cat} (sec^{-1})	0.017	0.006	ND	ND	0.006	0.003	ND
K_m (mM)	6.374	2.347	ND	ND	2.434	5.491	ND
k_{cat}/K_m (M^{-1} sec^{-1})	2.736	2.345	ND	ND	2.338	0.470	ND

Supplementary Table 7. Identification of cleavage products by mass spectrometry.

Analyte	Formula	Monoisotopic mass (Da)	Ion	Theoretical m/z	Measured m/z
c-hexaAMP					
c-hexaAMP	$C_{60}H_{72}N_{30}O_{36}P_6$	1974.3151	$[M-2H]^{2-}$	986.1497	986.1511
hexaAMP	$C_{60}H_{74}N_{30}O_{37}P_6$	1992.3257	$[M-2H]^{2-}$	995.1550	995.1553
pentaAMP	$C_{50}H_{62}N_{25}O_{31}P_5$	1663.2732	$[M-2H]^{2-}$	830.6288	830.6281
tetraAMP	$C_{40}H_{50}N_{20}O_{25}P_4$	1334.2207	$[M-2H]^{2-}$	666.1025	666.1027
triAMP	$C_{30}H_{38}N_{15}O_{19}P_3$	1005.1682	$[M-2H]^{2-}$	501.5762	501.5758
diAMP	$C_{20}H_{26}N_{10}O_{13}P_2$	676.1156	$[M-H]^{-}$	675.1078	675.1088
AMP	$C_{10}H_{14}N_5O_7P$	347.0631	$[M-H]^{-}$	346.0553	346.0548
c-tetraAMP					
c-tetraAMP	$C_{40}H_{48}N_{20}O_{24}P_4$	1316.2101	$[M-2H]^{2-}$	657.0972	657.0975
tetraAMP	$C_{40}H_{50}N_{20}O_{25}P_4$	1334.2207	$[M-2H]^{2-}$	666.1025	666.1016
triAMP	$C_{30}H_{38}N_{15}O_{19}P_3$	1005.1682	$[M-2H]^{2-}$	501.5762	501.5765
diAMP	$C_{20}H_{26}N_{10}O_{13}P_2$	676.1156	$[M-H]^{-}$	675.1078	675.1078
AMP	$C_{10}H_{14}N_5O_7P$	347.0631	$[M-H]^{-}$	346.0553	346.0554
c-triAMP					
c-triAMP	$C_{30}H_{36}N_{15}O_{18}P_3$	986.1575	$[M-2H]^{2-}$	492.5710	492.5710
triAMP	$C_{30}H_{38}N_{15}O_{19}P_3$	1005.1682	$[M-2H]^{2-}$	501.5762	501.5771
diAMP	$C_{20}H_{26}N_{10}O_{13}P_2$	676.1156	$[M-H]^{-}$	675.1078	675.1069
AMP	$C_{10}H_{14}N_5O_7P$	347.0631	$[M-H]^{-}$	346.0553	346.0554
pApA					
pApA	$C_{20}H_{26}N_{10}O_{13}P_2$	676.1156	$[M-H]^{-}$	675.1078	675.1108
AMP	$C_{10}H_{14}N_5O_7P$	347.0631	$[M-H]^{-}$	346.0553	346.0548
pApG					
pApG	$C_{20}H_{26}N_{10}O_{14}P_2$	692.1105	$[M-H]^{-}$	691.1027	691.1046
AMP	$C_{10}H_{14}N_5O_7P$	347.0631	$[M-H]^{-}$	346.0553	346.0547
GMP	$C_{10}H_{14}N_5O_8P$	363.0580	$[M-H]^{-}$	362.0502	362.0503
pGpG					
pGpG	$C_{20}H_{26}N_{10}O_{15}P_2$	708.1054	$[M-H]^{-}$	707.0976	707.0986
GMP	$C_{10}H_{14}N_5O_8P$	363.0580	$[M-H]^{-}$	362.0502	362.0509

Supplementary Table 8. SAXS data and parameters. Values of parameters for the samples are indicated above, and were determined under the indicated conditions. Parameters are defined in the main text.

	PorX	PorX + Zn^{2+}	PorX + Zn^{2+}	PorX-BeF_3
Concentration [mg/ml]	0.5, 2.0, 10.0	0.5	2.0	2.0
Buffer content	5 mM Tris pH 8.0, 150 mM NaCl	5 mM Tris pH 8.0, 150 mM NaCl and 43 µM $ZnCl_2$	5 mM Tris pH 8.0, 150 mM NaCl and 43 µM $ZnCl_2$	5 mM Tris pH 8.0, 150 mM NaCl, 15 mM $MgCl_2$, 30 mM NaF and 5 mM $BeSO_4$
q range [$Å^{-1}$]	0.009-0.5152	0.0137-0.5152	0.0147-0.5152	0.0487-0.5183
I_0 (Guinier)	82.9	41.4	58.2	20.1
I_0 (P(r))	79.9	41.3	57.7	18.7
Rg (Guinier) [Å]	30.9	35.6	39.1	34.5
Rg (P(r)) [Å]	29.6	35.6	39.0	33.4
Dmax [Å]	103	105	118	103
P(r) total estimate	0.854	0.859	0.855	0.942
P(r) chi^2 fit	1.09	1.05	1.06	1.07
Theoretical MW [kDa]	61.1	61.1	122.2	122.2
MW (Vc, qmax=0.2) [kDa]	58.2	61.6	115.8	117.7
MW (Vp)	59.7	54.6	121.7	122.1

Supplementary Table 9. Statistics of the *ab initio* DENSS maps.

	PorX-monomer	PorX-Dimer
Averaged map reconstructions	100	100
Resolution [Å] map average	34.0	49.0
Refinement steps	4184	10999
oversampling ratio	5	5
Final Chi^2	1.112e-01	5.540e-01
Final Rg [Å]	29.943	34.976
Final Support Volume[$Å^3$]	93526.900	186664.680

Supplementary references

1. Emsley, P., Lohkamp, B., Scott, W.G. and Cowtan, K. (2010) Features and development of Coot. *Acta Crystallogr D Biol Crystallogr*, **66**, 486-501.
2. Kato, K., Nishimasu, H., Oikawa, D., Hirano, S., Hirano, H., Kasuya, G., Ishitani, R., Tokunaga, F. and Nureki, O. (2018) Structural insights into cGAMP degradation by Ecto-nucleotide pyrophosphatase phosphodiesterase 1. *Nat Commun*, **9**, 4424.
3. Dohler, C., Zebisch, M. and Strater, N. (2018) Crystal structure and substrate binding mode of ectonucleotide phosphodiesterase/pyrophosphatase-3 (NPP3). *Sci Rep*, **8**, 10874.
4. Holm, L. (2020) DALI and the persistence of protein shape. *Protein Sci*, **29**, 128-140.
5. Agarwal, V., Borisova, S.A., Metcalf, W.W., van der Donk, W.A. and Nair, S.K. (2011) Structural and mechanistic insights into C-P bond hydrolysis by phosphonoacetate hydrolase. *Chem Biol*, **18**, 1230-1240.
6. Gorelik, A., Randriamihaja, A., Illes, K. and Nagar, B. (2017) A key tyrosine substitution restricts nucleotide hydrolysis by the ectoenzyme NPP5. *FEBS J*, **284**, 3718-3726.
7. Albright, R.A., Ornstein, D.L., Cao, W., Chang, W.C., Robert, D., Tehan, M., Hoyer, D., Liu, L., Stabach, P., Yang, G. *et al.* (2014) Molecular basis of purinergic signal metabolism by ectonucleotide pyrophosphatase/phosphodiesterases 4 and 1 and implications in stroke. *J Biol Chem*, **289**, 3294-3306.
8. Zalatan, J.G., Fenn, T.D., Brunger, A.T. and Herschlag, D. (2006) Structural and functional comparisons of nucleotide pyrophosphatase/phosphodiesterase and alkaline phosphatase: implications for mechanism and evolution. *Biochemistry*, **45**, 9788-9803.
9. Gorelik, A., Liu, F., Illes, K. and Nagar, B. (2017) Crystal structure of the human alkaline sphingomyelinase provides insights into substrate recognition. *J Biol Chem*, **292**, 7087-7094.
10. Morita, J., Kano, K., Kato, K., Takita, H., Sakagami, H., Yamamoto, Y., Mihara, E., Ueda, H., Sato, T., Tokuyama, H. *et al.* (2016) Structure and biological function of ENPP6, a choline-specific glycerophosphodiester-phosphodiesterase. *Sci Rep*, **6**, 20995.
11. UniProt, C. (2007) The Universal Protein Resource (UniProt). *Nucleic Acids Res*, **35**, D193-197.
12. Dennis, M.L., Newman, J., Dolezal, O., Hattarki, M., Surjadi, R.N., Nuttall, S.D., Pham, T., Nebl, T., Camerino, M., Khoo, P.S. *et al.* (2020) Crystal structures of human ENPP1 in apo and bound forms. *Acta Crystallogr D Struct Biol*, **76**, 889-898.
13. Jansen, S., Perrakis, A., Ulens, C., Winkler, C., Andries, M., Joosten, R.P., Van Acker, M., Luyten, F.P., Moolenaar, W.H. and Bollen, M. (2012) Structure of NPP1, an ectonucleotide pyrophosphatase/phosphodiesterase involved in tissue calcification. *Structure*, **20**, 1948-1959.

14. Kato, K., Nishimasu, H., Okudaira, S., Mihara, E., Ishitani, R., Takagi, J., Aoki, J. and Nureki, O. (2012) Crystal structure of Enpp1, an extracellular glycoprotein involved in bone mineralization and insulin signaling. *Proc Natl Acad Sci U S A*, **109**, 16876-16881.
15. Hausmann, J., Kamtekar, S., Christodoulou, E., Day, J.E., Wu, T., Fulkerson, Z., Albers, H.M., van Meeteren, L.A., Houben, A.J., van Zeijl, L. *et al.* (2011) Structural basis of substrate discrimination and integrin binding by autotaxin. *Nat Struct Mol Biol*, **18**, 198-204.
16. Bihani, S.C., Das, A., Nilgiriwala, K.S., Prashar, V., Pirocchi, M., Apte, S.K., Ferrer, J.L. and Hosur, M.V. (2011) X-ray structure reveals a new class and provides insight into evolution of alkaline phosphatases. *PLoS One*, **6**, e22767.